

Chapter 3

Plasmonic Modes of Annular Nanoresonators Imaged by Spectrally Resolved Cathodoluminescence

3.1 Applications of Annular Nanoresonators

Excitation and localization of surface plasmon polariton (SPP) modes in metallodielectric structures is currently a topic of intensive research motivated by the ability to achieve truly nanophotonic materials and devices with tunable optical dispersion [43]. In particular, nanoresonators are essential building blocks of future subwavelength-scale photonic systems as both active [44] and passive [45] device components. Nanostructures consisting of annular grooves and gratings in metal films exhibit exciting properties such as photon-to-plasmon coupling [46], focusing [47, 48, 49], and intensity enhancement [48, 49, 50]—all of which are exciting for sensing [51] and surface enhanced Raman scattering (SERS) applications [6, 52]. In this chapter, we directly excite plasmonic modes in engineered annular nanoresonators on Ag and Au surfaces with a highly localized electron beam source, and use spectrally resolved cathodoluminescence imaging [26] to probe the plasmon field intensity as a function of excitation position.

Surface plasmon polaritons are generally excited optically at a metal/dielectric interface using a prism or grating to couple the incident light to the surface wave [3]. Previously, annular gratings have been investigated with near-field optical techniques capable of 20 nm optical probe sizes [47, 49]. Alternatively, a focused electron beam

can be used to directly and locally excite SPPs with higher spatial resolution, without the intermediate step of generating and coupling an incident photon. Electron energy loss spectroscopy (EELS) in the transmission electron microscope (TEM) has been used to visualize plasmonic modes in metal nanoparticles, nanorods, and nanotriangles with spatial resolution limited only by the electron beam diameter, which can be as small as 1 nm [23, 27, 53, 54]. Such investigations in the TEM require samples to be electron transparent, e.g., to have thicknesses less than 100 nm. However, cathodoluminescence (CL) excitation in the scanning electron microscope (SEM) does not impose such a constraint on sample thickness. In the SEM, electron beam excitation yields CL emission which we used in Chapter 2 to investigate the propagation of SPPs along planar metal surfaces and linear gratings [55] (see also [56] and [29]). In this chapter, we extend this technique to investigate modes in nanofabricated plasmonic annular nanoresonators.

One possible application of an annular nanoresonator is illustrated schematically in Figure 3.1 as an electrically excited sensing platform for SERS. As the electron beam in an SEM acts as a prototypical means of electrically exciting surface plasmons, we imagine a chip-based sensing device that combines an electrical source of SPPs that propagate along the metal surface and are focused strongly using an annular nanoresonator. The enhanced local electric fields in the center of the resonator could significantly enhance the SERS signal, enabling a new sensor technology.

3.2 Fabrication and Experiment Setup

Nanoresonators were fabricated on Ag and Au surfaces. The Ag structures were prepared by evaporating 400 nm of Ag on a quartz substrate and using focused ion beam (FIB) nanofabrication with a Ga^+ ion source operating at 30 keV. Each annular resonator is composed of a center plateau and five concentric rings separated by grooves 50 nm deep, with varying grating ring period and center diameter. Nanoresonators with 15 concentric grooves 100 nm deep were also patterned in the (111) surface of a polished single crystal Au substrate grown by the Czochralski process.

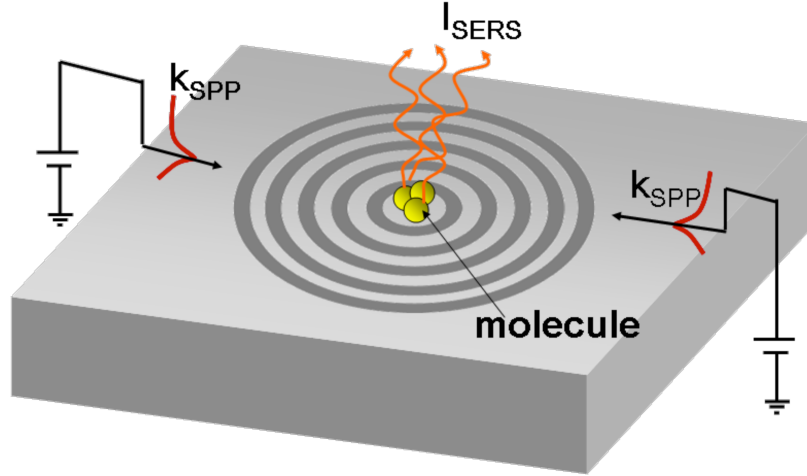


Figure 3.1. Schematic of a sensing device incorporating electrical excitation of surface plasmons that are focused to the center of an annular nanoresonator. Molecules located at the focal point will respond to the enhanced local fields, resulting in increased SERS intensity, I_{SERS} .

Spectrally resolved CL analysis was performed using a field emission SEM operating at 30 keV and equipped with a mirror-based cathodoluminescence detection system [26]. For this technique, the spatial resolution in excitation is limited only by the electron beam spot size of 5 nm. Monte Carlo simulations [42] of electron trajectories in a 400 nm thick Ag film on quartz are shown in Figure 3.2. As seen in the left image, although the electron trajectories extend entirely through the Ag film and beyond 4 μm into the SiO_2 substrate, any luminescence excited below several skin depths in the Ag film [11] is significantly attenuated before emission and detection are possible. Thus, any detected light arises only from interactions near the surface of the Ag film. Additionally, the enlargement of the interactions in the Ag film confirm that no significant beam broadening occurs within 20 nm of the Ag surface, one electric field skin depth. Therefore, this technique offers incredibly high spatial resolution in excitation.

When a metallic nanoresonator is excited with an electron beam, there are several phenomena that can result in light emission. High-energy electrons can directly

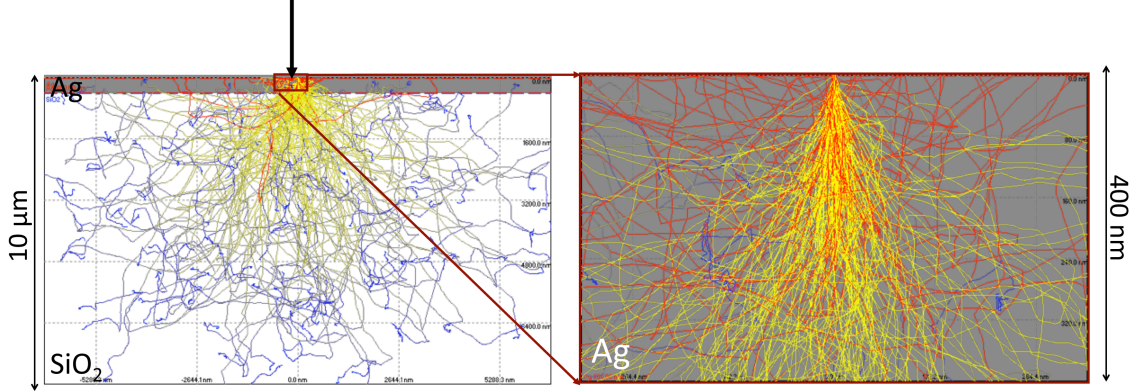


Figure 3.2. Left: Monte Carlo simulation [42] of 30 keV electron trajectories incident on a 400 nm thick Ag film on SiO₂. Right: Close-up of electron trajectories in Ag film, showing only slight beam broadening in the top 20 nm.

excite d-band transitions in the metal film, producing photons with energies of approximately 4 eV (310 nm) upon relaxation in Ag [57, 58]. The incident beam can also excite localized surface plasmons (SPs) and propagating SPPs. In the annular nanoresonator structures described here, the SPs can couple to resonant plasmonic modes. We show that such resonant modes are most efficiently excited by focusing the localized electron beam at positions corresponding to antinodes in the modal electric field intensity.

Light emitted from the sample is collected with a retractable paraboloidal mirror positioned above the sample (collection angle up to $\pm 80^\circ$ from the surface normal). For spectroscopy and spectrally resolved CL imaging of the Ag sample, emitted light is sent through a grating monochromator before being focused on the photomultiplier tube detector. For panchromatic imaging, the light emitted from the sample is focused directly onto the photomultiplier detector, detecting photons with wavelengths ranging from 300 to 900 nm. Spectrally resolved CL images are obtained by setting the grating monochromator to a specific wavelength and scanning the electron beam over a selected area of the sample with a per pixel dwell time of 10 ms and a passband of 27 nm. Secondary electron and CL images are obtained simultaneously. The images were postprocessed to correct for the drift in the scan direction by shifting each

row of pixels of the SEM image to recreate the true annular resonator topography, and applying this same correction to the corresponding CL image. Any drift in the vertical direction is not corrected, explaining the elongated center region in several of the images. The single crystal Au sample was imaged using spectral detection on a CCD array detector, sampling wavelengths from 387 to 947 nm. Spectrally resolved images are obtained by taking slices through the compiled image with 20 nm spectral resolution.

3.3 Determining Modes of Annular Nanoresonators

We employ two different simulation methods to investigate the plasmonic modes of annular nanoresonators. Finite difference time domain (FDTD) calculations allow us to determine resonant frequencies and electric field profiles of each mode. With the boundary element method (BEM), we are able to calculate the probability of CL emission in an annular nanoresonator. Ultimately, these results are compared with the experimental results in Section 3.4.

3.3.1 Finite Difference Time Domain (FDTD)

First, we perform three-dimensional full-field electromagnetic simulations that solve Maxwells equations using the finite difference time domain (FDTD) method [59]. We assume that the optical constants of Ag are described by the Drude model:

$$\varepsilon(\omega) = \varepsilon_h - \frac{(\varepsilon_s - \varepsilon_h)\omega_p^2}{\omega^2 + i\omega\nu_c}, \quad (3.1)$$

with relative permittivity in the static limit $\varepsilon_s = 6.18$, relative permittivity in the high-frequency limit $\varepsilon_h = 5.45$, plasma frequency $\omega_p = 1.72 \times 10^{16}$ rad·s⁻¹, and the collision frequency $\nu_c = 8.35 \times 10^{13}$ rad·s⁻¹. We simulate a structure with 600 nm center diameter and 300 nm grating period using a cylindrical slab of Ag (400 nm thick, 4 μ m diameter) containing annular grooves (50 nm deep, 150 nm wide, spaced 150 nm apart) all enclosed in a matrix of air. A propagating plane wave incident

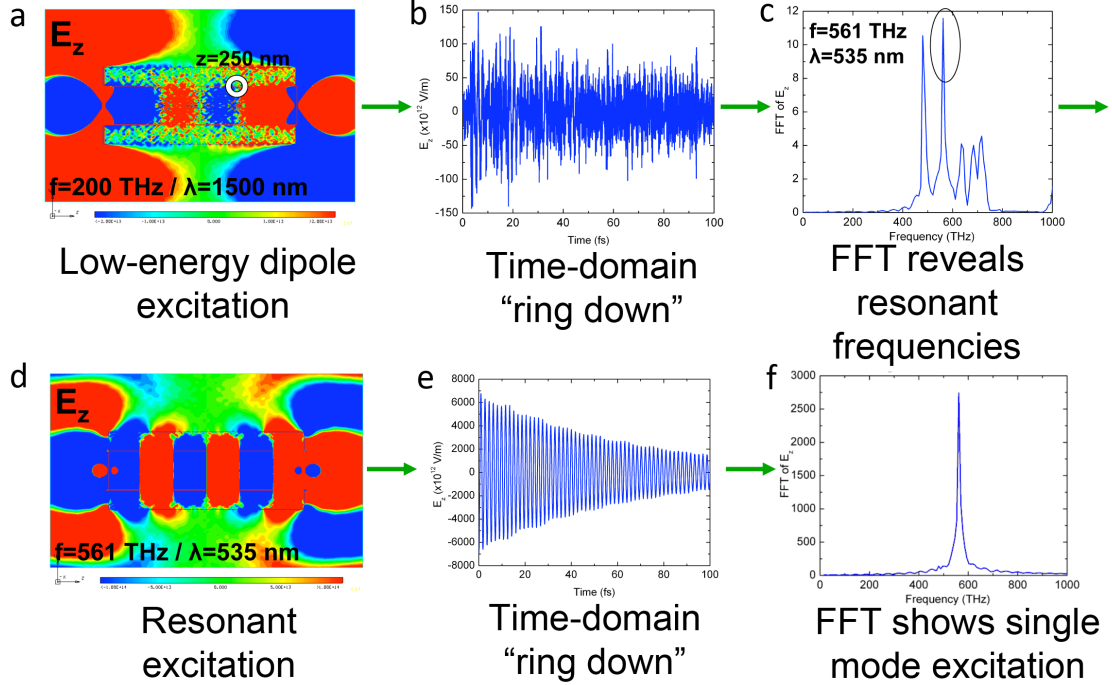


Figure 3.3. Method of determining resonant modes with FDTD, illustrated using a SiO_2/Ag core-shell nanowire resonator. (a) First, we excite with a low-frequency source, here dipoles at 200 THz or 1500 nm. (b) After 100 fs, the source is effectively turned off, and the fields in the resonator “ring down” for 100 fs. (c) A fast-Fourier transform (FFT) of the time-domain data reveals the resonant frequencies. (d) Exciting on resonance and (e) subsequent ring down demonstrates (f) single-mode excitation.

normal to the Ag surface is used as the source, polarized along an arbitrary direction in the plane of the surface. A two-step process is used to identify the resonant modes and their corresponding frequencies [60], illustrated in Figure 3.3. A SiO_2/Ag core-shell nanowire is used in this example. Here, the resonator is first excited with low-energy dipoles (frequency of 200 THz or $\lambda = 1500$ nm) at both ends of the wire, shown in Figure 3.3a. This distributes energy into all of the resonant modes. Then, after driving the structure at this frequency for 100 fs, the excitation source is turned off, leaving only the induced fields in the resonator. The structure is allowed to decay, or “ring down” for a period of 100 fs and the electric fields as a function of

time are monitored at specific locations in the resonator (marked with the white circle in Figure 3.3a). This time domain data is plotted in Figure 3.3b, a superposition of the decay from many modes. A fast-Fourier transform (FFT) of the time-domain data reveals clear peaks corresponding to the various resonant modes of the structure that are seen in Figure 3.3c. Selecting a specific mode, here the peak at the frequency $f = 561$ THz or $\lambda = 535$ nm, we then excite on-resonance with dipoles (Figure 3.3d) and again turn off the source to observe the time-domain decay. Figure 3.3e shows characteristic resonant decay, and a FFT of the time-domain data confirms single-mode excitation (Figure 3.3f). The time-domain ring down after resonant excitation also allows us to calculate the quality factor Q of the resonator. A single-exponential decay is fitted to the decay of $|E_x|^2$, and the decay constant τ is related to the quality factor by

$$Q = 2\pi f\tau. \quad (3.2)$$

For the Ag nanoresonators, the structure is first excited non-resonantly with a low-energy plane wave. The excitation is then turned off, and the induced electric fields ring down, allowing the resonator to select its natural frequencies in the absence of an external driving field. This method of illumination effectively contains a wide spectral intensity that is peaked around the frequency of the initial plane wave. Following the method of Figure 3.3, the time domain ring down data reveals the frequency response. Cathodoluminescence imaging spectroscopy is not a time-resolved technique, and a valid comparison between experimental results and simulations must include observables that are averaged over at least one optical cycle. The time-averaged electric field intensity was determined by squaring the magnitude of 25 three-dimensional electric field snapshots from a single time period at the end of the simulation, and averaging the result. Resonator modes with symmetries that are not supported by normal-incidence excitation were investigated with off-axis plane waves. The incident angle was chosen to impose the correct symmetry upon the center region of the nanoresonator.

3.3.2 Boundary Element Method (BEM)

Boundary element method (BEM) simulations [61, 62] allow us to calculate the probability of cathodoluminescence emission for various positions in the annular nanoresonators. Computations are performed in the frequency domain, where the electromagnetic field within each homogeneous region of space is expressed in terms of auxiliary boundary charges and currents. The customary boundary conditions are used to obtain a set of surface-integral equations involving those boundary sources, which are solved using linear-algebra techniques upon discretization of the boundaries via a set of representative surface points. Furthermore, the axial symmetry of the annular resonators is used to decompose the fields in uncoupled azimuthal components m with azimuthal-angle dependence as $e^{im\phi}$. This results effectively in a one-dimensional field calculation problem that is solved with great accuracy. Converged results for a nanoresonator of 600 nm center diameter and 300 nm period have been achieved using ~ 1000 discretization points. Calculated CL intensities are obtained using as an external source the field of a 30 keV electron, which is separated analytically in frequency components. The integral of the time-averaged Poynting vector over emission directions in the far field for each frequency component yields the CL intensity at that particular photon frequency. Tabulated optical data has been used as input for the dielectric function [34].

3.3.3 Resonant Modes

Full-field FDTD simulations are used to determine the plasmonic modes of an Ag annular nanoresonator with 600 nm center diameter and 300 nm grating ring period. We adopt a naming convention for the modes $M_{k,n}$, where the integer k refers to the symmetry of the mode ($k = 0$ for modes with nodes in electric field intensity in the center, and $k = 1$ for modes with intensity antinodes in the center) and the integer n denotes the number of intensity antinodes in the radial direction of the center plateau, extending outwards from the center of the structure and excluding peaks at the edges. These modes are shown schematically in Figure 3.4.

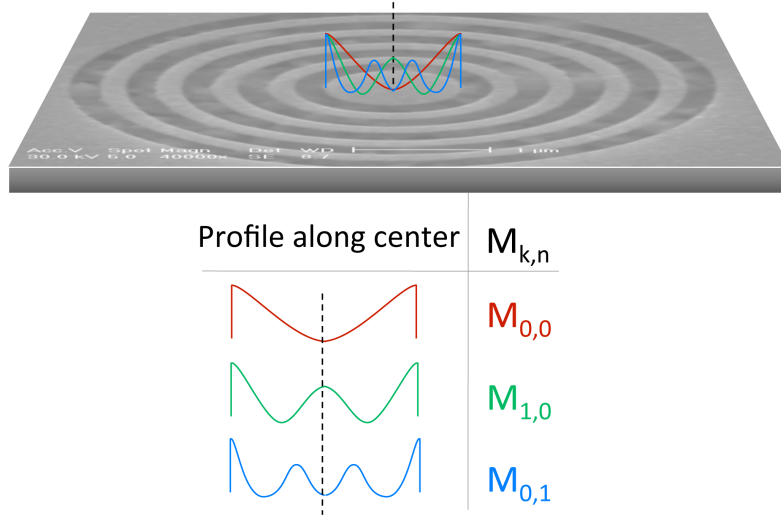


Figure 3.4. Schematic illustration of modes supported by annular nanoresonators. The naming convention $M_{k,n}$ is used to describe both the symmetry of the mode (k) and the number of antinodes along the center (n).

The FFT spectra for low-energy normal incidence plane-wave excitation at $\lambda = 1500$ nm in Figure 3.5a shows multiple features, including a peak at $\lambda = 330$ nm corresponding to the Ag surface plasmon resonance [11] and two broad peaks: one centered at $\lambda = 430$ nm and one in the 700–900 nm range.

Subsequent excitation in each of these two bands at $\lambda = 723$ nm (mode $M_{0,0}$, Figure 3.5b) and $\lambda = 430$ nm (mode $M_{0,1}$) leads to strong resonant response that we therefore attribute to plasmonic modes of the nanoresonator, with symmetry indicated in Figure 3.4. Off-axis plane wave excitation enables investigation of an additional spectral peak centered at $\lambda = 600$ nm (mode $M_{1,0}$), shown in the bottom figure of Figure 3.5b. Symmetry forbids excitation of this mode at normal incidence in our simulation, but off-normal incidence plane wave excitation breaks this symmetry constraint, and an antinode in electric field intensity is observed at the center. Characterizing the quality of these plasmonic nanoresonators is essential for development of future devices. We determine the quality factor [63] Q of the nanoresonator for each mode by (3.2) from the exponential decay time of the electric field intensity

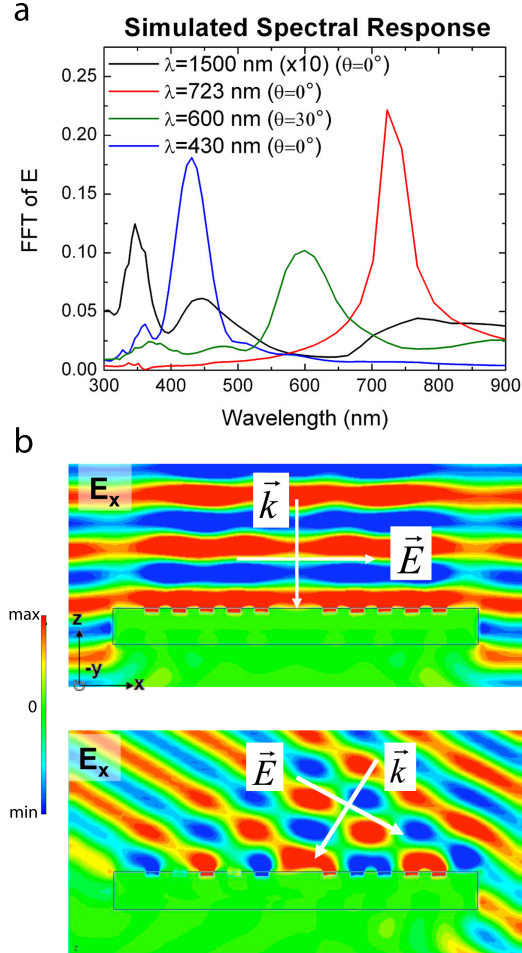


Figure 3.5. Determining modes with FDTD. (a) Simulated spectral-response for an Ag annular nanoresonator with 600 nm center diameter and 300 nm pitch for plane-wave excitation at the indicated wavelength and angle with respect to the normal. (b) Cross-sectional E_x profiles for plane wave excitation at normal incidence (top) and at $\theta = 30^\circ$ (bottom).

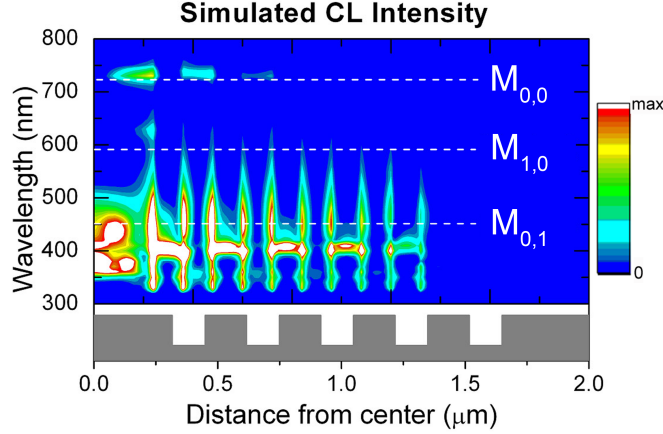


Figure 3.6. Boundary element method simulations of plasmonic modes of an Ag nanoresonator. Probability of cathodoluminescence emission is plotted as a function of excitation wavelength and position at a distance of 10 nm above the Ag topmost surface. Modes $M_{0,0}$, $M_{1,0}$, and $M_{0,1}$ are indicated at wavelengths of $\lambda = 720$ nm, $\lambda = 590$ nm, and $\lambda = 450$ nm, respectively.

during ring down, giving $Q_{0,0} = 36$, $Q_{1,0} = 18$, and $Q_{0,1} = 8$.

Using BEM simulations, we calculate the probability of cathodoluminescence emission as a function of electron beam position for this same structure. Figure 3.6 shows CL intensity as a function of both distance from the annular nanoresonator center and wavelength of emitted light. The CL probability is calculated by integrating the emission for directions from the grating normal up to 30° from the normal. At $\lambda = 720$ nm, bright CL intensity is concentrated only at the edge of the center plateau, characteristic of $M_{0,0}$. Mode $M_{1,0}$ is observed at $\lambda = 590$ nm, characterized by a small peak in emitted intensity at the center of the structure. At $\lambda = 450$ nm, a node in CL intensity in the center of the structure and one antinode along the radial direction distinguishes $M_{0,1}$. For this mode, bright CL emission is also localized at the edges of the center and concentric rings.

3.4 Imaging Modes Using Cathodoluminescence

We now investigate annular nanoresonators experimentally using CL imaging spectroscopy. The fabrication and experiment setup were described in Section 3.2.

3.4.1 Panchromatic CL Imaging

Figure 3.7 shows panchromatic CL images of nanoresonators in Ag with 315 nm grating period and three different center diameters. The CL images represent the radiation collected from the entire resonator as a function of the electron beam excitation position on the structure. Bright regions in the images correspond to greater emitted photon intensity. For all annular nanoresonators shown here, we see high intensity for excitation at the edges of the center as well as the concentric rings. The locally increased emission inside the grooves is attributed to scattering from roughness in the polycrystalline Ag film, formed because of the crystal orientation-dependent focused ion beam milling rate. The intensity line profiles in Figure 3.7e correspond to the dashed lines through the panchromatic CL image in Figure 3.7c and the correlated SEM image in Figure 3.7d. The CL profile clearly shows peaks in emission when the electron beam dwells near an edge. An overall decay in emission intensity is observed as the electron beam moves outward from the center. Thus, we see that a higher emitted photon intensity is obtained for electron beam excitation in the center of the structure, indicating that more efficient excitation and/or more efficient outcoupling occurs in this region.

3.4.2 Imaging Modes of an Ag Nanoresonator

Spectrally resolved CL imaging was used to experimentally reveal the plasmonic modes discussed in Section 3.3. Figure 3.8 shows SEM and spectrally resolved CL images of an annular resonator with a 620 nm center diameter and 315 nm grating period. At $\lambda = 350$ nm, very close to the Ag surface plasmon resonance, nearly uniform emission occurs for excitation anywhere in the structure. Near resonance, surface plasmon propagation lengths are very short, and thus no resonator modes can

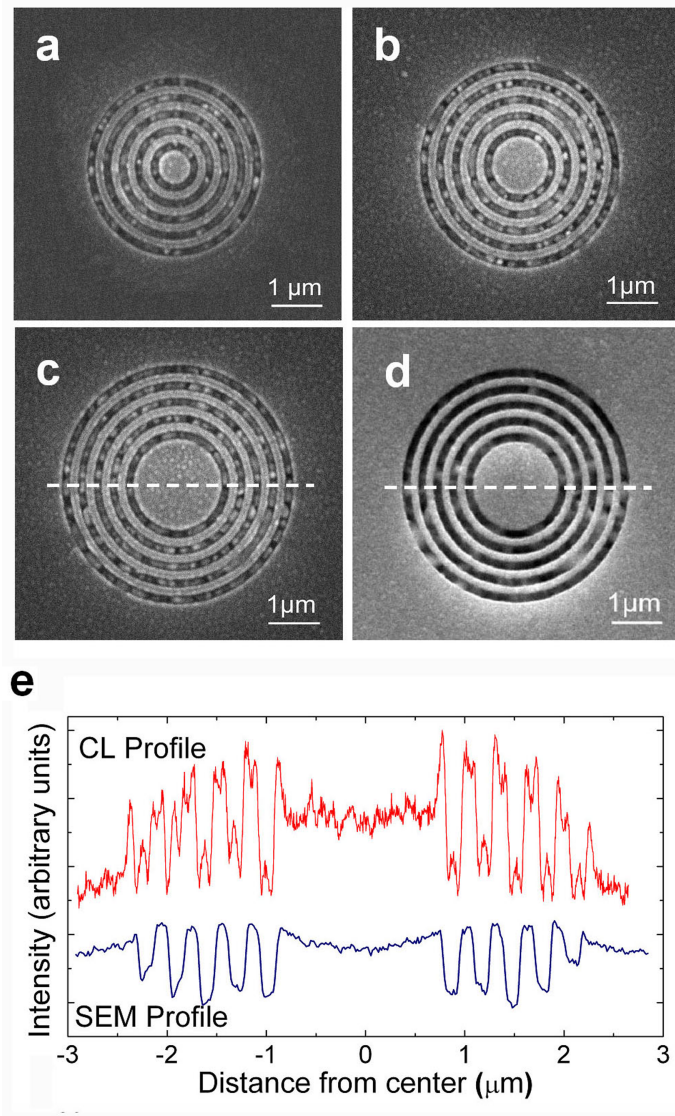


Figure 3.7. Panchromatic CL imaging of Ag annular nanoresonators with 315 nm period and center sizes of (a) 620 nm, (b) 1.07 μm , and (c) 1.70 μm . (d) SEM image taken concurrently with panchromatic CL image of structure in (c). (e) Line profiles from regions indicated by the dashed line in (c) and (d) illustrating strong emission when the electron beam is positioned at an edge and decreasing intensity as the beam moves outward from the center.

build up. Several different modes are observed at longer wavelengths, illustrated in Figure 3.8c. Line profiles of the simulated time-averaged electric field intensity from FDTD and the BEM-calculated probability of CL emission are plotted alongside experimental CL emission profiles for $\lambda = 500$ nm, $\lambda = 600$ nm, and $\lambda = 700$ nm. At $\lambda = 700$ nm, CL data show bright emission for excitation near the edges of the center plateau, but uniform emission from the rest of the structure. This is consistent with excitation of $M_{0,0}$, where high fields are localized at the edges of the center region and not in the surrounding rings. Mode $M_{1,0}$, imaged at $\lambda = 600$ nm, is characterized by an antinode in the resonator center that is captured in experimental and simulated line profiles. The onset of $M_{0,1}$ is observed at $\lambda = 500$ nm, with four peaks in the center region revealed in the CL linescan. These regions of enhanced emission in the center plateau correlate well with the simulated electric field intensity and CL profiles.

CL images and corresponding near-field $|\mathbf{E}|^2$ images from FDTD calculations are shown in Figure 3.9. Simulations require polarized excitation, whereas cathodoluminescence emission is unpolarized. Therefore, the images must be compared across the center (along the direction of polarization), indicated by the dashed white lines and plotted in Figure 3.8c. We also note that for modes $M_{0,0}$ and $M_{0,1}$, the best agreement between simulated and experimentally imaged modes is found for slightly different wavelengths. This can be attributed to uncertainty in parameterization of the effective dielectric function in the grooves of the fabricated Ag nanoresonators. The FIB milling of polycrystalline Ag leads to very rough surfaces in the grooves, preventing accurate representation of the groove depth and profile in simulations. The remaining spectrally resolved CL images in Figure 3.8a can be understood primarily as superpositions of $M_{0,0}$, $M_{1,0}$ and $M_{0,1}$.

3.4.3 Imaging Modes of an Au Nanoresonator

To further explore higher order modes in plasmonic nanoresonators, larger structures were fabricated in single crystal Au (Figure 3.10a). The absence of grain boundaries and hence longer propagation lengths enable clear observations of modes in larger

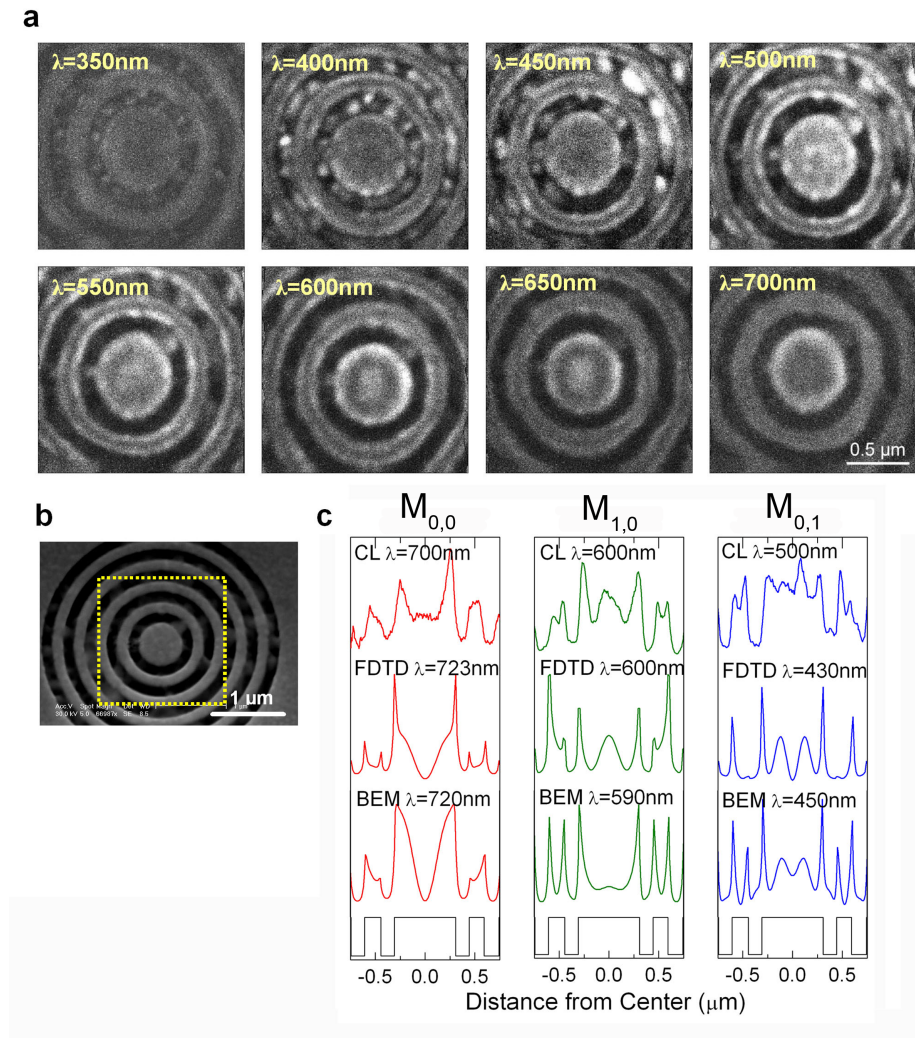


Figure 3.8. Spectrally resolved imaging of plasmonic modes in an Ag annular nanoresonator with 620 nm center diameter and 315 nm grating period. (a) Spectrally resolved CL images at the indicated wavelengths, each 350×350 pixels² with a per pixel dwell time of 10 ms and 27 nm spectral passband. (b) SEM image of nanoresonator indicating the scan region for the CL images in (a). (c) Line profiles of modes $M_{0,0}$, $M_{1,0}$, and $M_{0,1}$ from FDTD simulated time-averaged electric field intensity, probability of CL emission from BEM simulations, and spectrally resolved CL images at the indicated wavelengths. The corresponding surface topography is shown in gray.

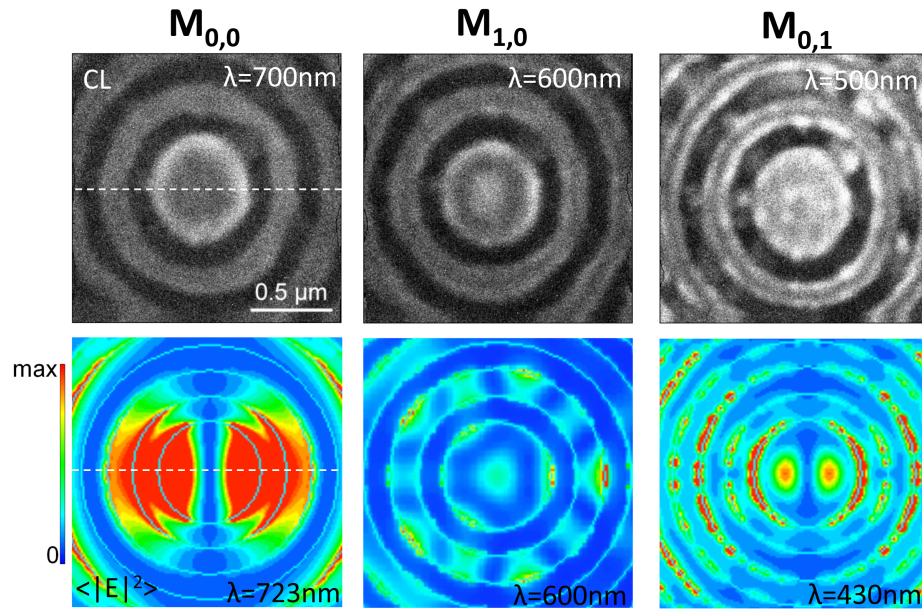


Figure 3.9. (top) CL images of modes $M_{0,0}$, $M_{1,0}$, and $M_{0,1}$ taken at the indicated wavelengths, and (bottom) time-average near-field electric field intensity maps from plane-wave excitation at the indicated wavelengths. Excellent agreement is found when comparing the intensities along the center of the images (indicated by the dashed white line).

resonators. Figure 3.10a shows spectrally resolved CL images of a resonator with a 2.6 μm center plateau surrounded by 15 concentric grooves with 250 nm grating period. The experimental line profiles in Figure 3.10b indicate that the CL emission along the center region varies with wavelength, showing modes with 5, 6, and 7 antinodes at wavelengths of $\lambda = 798$ nm ($M_{1,2}$), $\lambda = 720$ nm ($M_{0,3}$), and $\lambda = 661$ nm ($M_{1,3}$) respectively. The probability of CL emission is calculated from BEM simulations of this Au resonator, with the number of grooves truncated at five. Simulated CL intensity line profiles at wavelengths of $\lambda = 800$ nm, $\lambda = 730$ nm, and $\lambda = 660$ nm are also plotted in Figure 3.10b. Although the scan area of $5 \times 5 \mu\text{m}^2$ prevents experimentally resolving the simulated peaks in emission intensity at the edges of the grooves, excellent agreement is found between spatial variation of the experimental and calculated CL intensity along the center region for each mode.

3.5 Chapter Summary

In this chapter, we have demonstrated high-resolution spectrally resolved cathodoluminescence imaging as a powerful tool to reveal plasmonic modes in Ag and Au annular nanoresonators. Boundary element method calculations of the CL emission characteristics for each resonator mode agree very well with experimental results. Further, we have used full-field electromagnetic simulations to identify the plasmonic modes of Ag nanoresonators, and we have proposed a direct correlation between the luminescence emission intensity and electron beam excitation at antinodes of the electric field intensity corresponding to particular plasmonic modes.

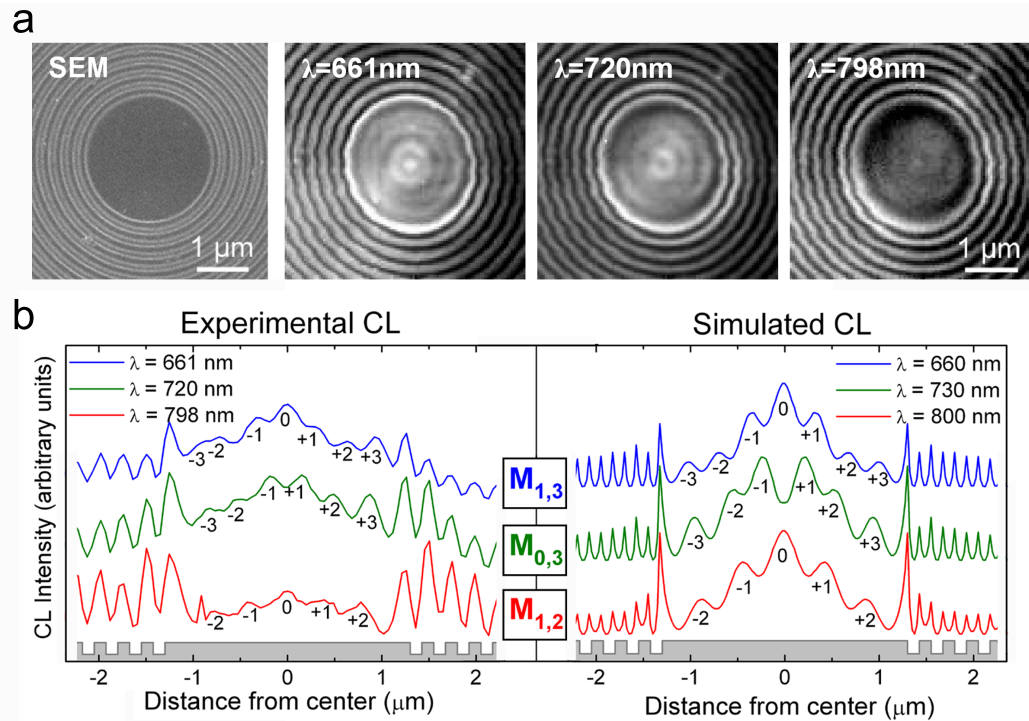


Figure 3.10. Imaging modes in a single-crystal Au nanoresonator with $2.6\ \mu\text{m}$ diameter center plateau surrounded by 15 grooves with $250\ \text{nm}$ grating ring period and $100\ \text{nm}$ groove depth. (a) SEM image of nanoresonator and spectrally resolved CL images at the indicated wavelengths. (b) Line profiles of modes $M_{1,3}$, $M_{0,3}$, and $M_{1,2}$ from spectrally resolved CL images and simulated CL intensity along the center of the resonator in (a). Experimental line traces at the designated wavelengths are obtained by summation over 4 pixel lines in the horizontal direction, corresponding to a $193\ \text{nm}$ line width. Simulated CL intensity is calculated from BEM simulations. The peaks in CL intensity along the center region are numbered for both experimental and simulated line profiles. Surface topography is shown in gray.